

MIT Open Access Articles

*Underwater Sound Characteristics of a  
Ship with Controllable Pitch Propeller*

The MIT Faculty has made this article openly available. **Please share** how this access benefits you. Your story matters.

**Citation:** Journal of Marine Science and Engineering 10 (3): 328 (2022)

**As Published:** <http://dx.doi.org/10.3390/jmse10030328>

**Publisher:** Multidisciplinary Digital Publishing Institute

**Persistent URL:** <https://hdl.handle.net/1721.1/141117>


**Version:** Final published version: final published article, as it appeared in a journal, conference proceedings, or other formally published context

**Terms of use:** Creative Commons Attribution



Article

# Underwater Sound Characteristics of a Ship with Controllable Pitch Propeller

Chenyang Zhu <sup>1,\*</sup>, Tomaso Gaggero <sup>2</sup> , Nicholas C. Makris <sup>1</sup> and Purnima Ratilal <sup>3</sup>

<sup>1</sup> Department of Mechanical Engineering, Massachusetts Institute of Technology, Cambridge, MA 02139, USA; makris@mit.edu

<sup>2</sup> Department of Electrical, Electronic, Telecommunication Engineering and Naval Architecture (DITEN), University of Genova, 16145 Genova, Italy; tomaso.gaggero@unige.it

<sup>3</sup> Department of Electrical and Computer Engineering, Northeastern University, Boston, MA 02115, USA; purnima@ece.neu.edu

\* Correspondence: czhu1230@mit.edu

**Abstract:** The time-dependent spectral characteristics of underwater sound radiated by an ocean vessel has complex dependencies on ship machinery, propeller dynamics, hydrodynamics of ship exhaust and motion, as well as ship board activities. Here the underwater sound radiated by a ship equipped with a controllable pitch propeller (CPP) is analyzed and quantified via its (i) power spectral density for signal energetics, (ii) temporal coherence for machinery tonal sound, and (iii) spectral coherence for propeller amplitude-modulated cavitation noise. Frequency-modulated (FM) tonal signals are also characterized in terms of their frequency variations. These characteristics are compared for different propeller pitch ratios ranging from 20% to 82% at fixed propeller revolutions per minute (RPM). The efficacy and robustness of ship parameter estimation at different pitches are discussed. Finally, analysis of one special measurement is provided, when ship changes speed, propeller pitch and RPM over the duration of the measurement. The 50% pitch is found to be a crucial point for this ship about which tonal characteristics of its underwater radiated sound attain their peak values, while broadband sound and associated spectral coherences are at a minimum. The findings here elucidate the effects of pitch variation on underwater sound radiated by ships with controllable pitch propellers and has applications in ship design and underwater noise mitigation.

**Keywords:** ship-radiated underwater sound; ship noise; controllable pitch propeller; power spectra; coherence; ship parameters; robustness; passive ocean acoustic waveguide remote sensing



**Citation:** Zhu, C.; Gaggero, T.; Makris, N.C.; Ratilal, P. Underwater Sound Characteristics of a Ship with Controllable Pitch Propeller. *J. Mar. Sci. Eng.* **2022**, *10*, 328. <https://doi.org/10.3390/jmse10030328>

Academic Editor: Decheng Wan

Received: 9 January 2022

Accepted: 17 February 2022

Published: 25 February 2022

**Publisher's Note:** MDPI stays neutral with regard to jurisdictional claims in published maps and institutional affiliations.



**Copyright:** © 2022 by the authors. Licensee MDPI, Basel, Switzerland. This article is an open access article distributed under the terms and conditions of the Creative Commons Attribution (CC BY) license (<https://creativecommons.org/licenses/by/4.0/>).

## 1. Introduction

Examining, characterizing, and monitoring the underwater sound radiated from a ship is important to many oceanic applications. These include ship health monitoring for prevention of shipboard machinery and structural failures, underwater environmental noise mitigation from man-made vehicles, as well as maritime surveillance and defence [1–9]. The sound radiated from an ocean vessel can limit detection ranges in both passive and active sonar systems for a wide range of ocean remote sensing applications [1,9–19], as well as in ocean acoustic communication [20,21]. It may also impact the behavior and communication of marine organisms [22–26], such as fish [13,27–31] and marine mammals [32,33].

The mechanisms for the sound generated by ships are described in [9,29,34–39]. The sources of ship-radiated underwater sound include (i) persistent onboard machinery, such as engines and air-conditioning systems, (ii) propulsion dynamics, such as propeller and shaft rotation, (iii) hydrodynamical effects, such as cavitation, vortex shedding, intakes and exhausts, and (iv) other time-limited or transient activities, such as cargo handling and mooring and slamming motions [4,9]. Machinery and propeller noise dominate a ship's radiated underwater sound [9]. The overall underwater sound emanated by a ship comprises colored broadband noise over a wide frequency range embedded with several prominent narrowband tonal

components from onboard machinery, along with time-varying and amplitude-modulated sound pressure levels due to propeller rotation.

Here, we analyze and characterize the underwater sound radiated by a specific ship with a controllable pitch propeller (CPP) and received on three vertically deployed hydrophones. The ship-radiated underwater sound characterization follows the approach of Refs. [40,41] and includes the calculation of (i) the power spectral density (PSD) for broadband sound energetics, (ii) the temporal coherence for machinery tonal sound, and (iii) the spectral coherence for amplitude-modulated propeller cavitation noise. The frequency variations of frequency-modulated (FM) tonal signals that are probably due to the non-uniform wake from the propeller blades caused by the ship's physical motions, such as yaw, roll or pitch, are also quantified. The calculations are initially made on measurements with ship at fixed propeller pitch ratio and revolutions per minute (RPM). These features are then compared for different propeller pitch ratios ranging from 20% to 82% at a fixed RPM. The 50% propeller pitch ratio was found to be a crucial point, at which multiple features of ship noise attain either their peak or minimum values. The efficacy and robustness of the ship parameter estimation at different pitches are discussed. Finally, an analysis of one special measurement is provided when the ship's speed, propeller pitch, and RPM are varied over the duration of the measurement.

Studies of the effects of propeller pitch variation on the underwater sound radiated by ships with controllable pitch propellers are limited since most previous works analyzed data from ships with fixed-pitch propellers. The underwater sound radiated by small ships is analyzed in [39,42,43], while that from large commercial ships, including tanker, carrier, cargo, and container ships, is compared and quantified in terms of source level and spectral shape in [44]. Approaches for quantifying the cyclostationarity of ship propeller noise are developed in [45,46].

Underwater ship-radiated sound analyses in the published literature are often based on single hydrophone measurements. Other sensing modalities that deploy more than a single hydrophone have been implemented. In [4], ship cavitation noise was analyzed using the Stevens Passive Acoustic Detection System (SPADES) with two crossed pairs of hydrophones deployed near a harbour. A large aperture, densely-sampled coherent hydrophone array with 160-elements was employed to analyze the underwater sound radiated from multiple ships using the Passive Ocean Acoustic Waveguide Remote Sensing (POAWRS) technique over instantaneous wide areas, with >100 km diameters, in several continental shelf environments [40,41,47,48]. The analysis was focused on the detection and characterization of ship tonal signals, as well as passive ship localization in [47,48]. Three different approaches were applied to the POAWRS dataset in [40,41] for the simultaneous and automatic detection, bearing-time estimation, and acoustic signature characterization of multiple ships over long ranges, which included broadband energetics, temporal coherence for tonal extraction, and spectral coherence for cyclostationary propeller cavitation noise analysis.

Models of ship-radiated underwater sound spectra for a wide range of ships are useful in ship design and enhancement, sonar performance prediction, and modeling the impact of ship noise on communication between marine fauna. In [49], ship noise spectral levels predicted using empirical models were compared to measurements for several ships. In [50,51], a parametric analysis of the noise spectra radiated by commercial ships operating in different conditions was developed. A new spectral parametrization model was proposed that delivers a better performance than traditional methods due to greater model flexibility, based on calibration with empirical data. These analyses included ships with controllable pitch propellers, one of which is analyzed here for signature characterization in terms of propeller pitch ratios.

## 2. Data Collection

The acoustic data were acquired in an experimental campaign carried out within the framework of EU FP7 collaborative projects AQUO [52]. The measurement procedure

followed the ANSI/ASA standard [53]. The ship-radiated underwater sound was received on buoy-mounted hydrophones (see Figure 1a) [49]. The ship under test passed the hydrophone array in a straight course at different operative conditions and different lateral distances (see Figure 1b). The ship’s course and speed were kept constant from the COMEX to FINEX points. The underwater acoustic data was recorded on the hydrophones during the time window from the “Start Data” to “End Data” points identified in Figure 1, spanning a 30 degree angle on both sides of the closest point of approach.

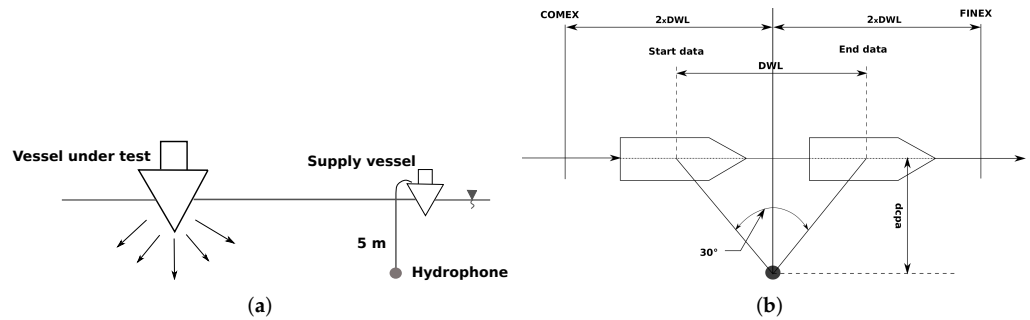


**Figure 1.** Measurement geometry for the ship-radiated underwater sound received on a vertical hydrophone array, in (a) side view and (b) top view. The straight line distance traversed by the target ship while the data was being recorded is represented by DWL. The horizontal distance from the target ship to the hydrophone at the closet point of approach is represented by dcpa. (DWL = 136.9 m, dcpa = 118.6 m).

For the present study, only data acquired by the top hydrophone was analyzed. The sampling frequency was 13.11 kHz. The ship used for the experimental campaign was the research vessel (RV) Navigator XXI, equipped with a controllable pitch propeller (CPP). The basic physical properties of this vessel are listed in Table 1, while the ship’s propeller and engine parameters are provided in Tables 2 and 3, respectively.

The ship’s machinery rotation parameters were obtained, including cylinder firing rate  $CFR$ , engine firing rate  $EFR$ , propeller shaft frequency  $SF$ , and propeller blade pass frequency  $BPF$ , as shown in Table 4. These parameters were calculated as follows:

$$CFR_n = \frac{RPM_e}{60} \cdot \frac{2}{N_s} \cdot n \tag{1}$$

$$EFR_n = CFR_1 \cdot N_c \cdot n \tag{2}$$

$$SF_n = \frac{RPM_p}{60} \cdot n = \frac{RPM_e / RGR}{60} \cdot n \tag{3}$$

$$BPF_n = SF_1 \cdot N_b \cdot n, \tag{4}$$

where  $n$  represents the  $n$ th harmonic order number,  $RPM_e$  is the engine RPM,  $RPM_p$  is the propeller RPM,  $RGR$  is the reduction gear rate,  $N_c$  is the number of cylinders,  $N_s$  is the number of strokes, and  $N_b$  is the number of blades on the propeller.

**Table 1.** The basic parameters of the ship.

Name	Type	Length	Breadth	Draught (fore)	Draught (aft)	Depth	Displacement
Navigator XXI	Research vessel	60.30 m	10.50 m	3.15 m	3.20 m	4.20 m	1126 m <sup>3</sup>

**Table 2.** The parameters of the ship’s propeller.

Propeller Type	Number	Pitch (%)	Blade Number	Model	Location from aft (Perpendicular)
CPP	1	20–82%	4	abb zamech type p680/4-rps5000 conventional/clt/high skew	3 m

**Table 3.** The parameters of the ship’s engine.

Engine Type	Number	Cylinder Number	Stroke Number	Reduction Gear Rate (RGR)	RPM
Diesel (Conventional)	1	8	4	3.75	760

**Table 4.** The parameters of the ship’s machinery rotation.

Cylinder Firing Rate (CFR) Hz	Engine Firing Rate (EFR) Hz	Shaft Frequency (SF) Hz	Blade Pass Frequency (BPF) Hz
6.3	50.7	3.37	13.51

### 3. Ship-Radiated Underwater Sound Analysis Methods

Underwater sound radiated by a ship is a complex superimposition of both broadband noise, mainly due to cavitation and the flow around the hull, and tonal components with specific frequencies due to the periodicity of on-board machinery and the propulsion system. Consequently, different techniques can be used to highlight different characteristics of the sound emitted by a ship. Here, we employed the approaches of Refs. [40,41] to analyze the underwater acoustic hydrophone data containing ship-radiated sound from RV Navigator XXI with a controllable pitch propeller, as described below.

#### 3.1. Power Spectral Density for Signal Energetics

Traditional power spectral density (PSD) is calculated to reveal signal’s power distribution across a broad frequency band. The spectral curve variations reveal the features of ship-radiated broadband noise. Energetic narrowband tonal signal components can also be observed in signal PSD, especially at low frequencies below 2 kHz. The Welch’s averaged modified periodogram method [54] was used to estimate PSD:

$$A_k(n) = \frac{1}{L} \sum_{j=0}^{L-1} x_k(j)w(j)e^{-j2\pi in/L} \tag{5}$$

$$I_k(f_n) = \frac{L}{U} |A_k(n)|^2 \quad k = 1, 2, \dots, K \tag{6}$$

$$f_n = \frac{n}{L} \quad n = 0, \dots, L/2 \tag{7}$$

$$U = \frac{1}{L} \sum_{j=0}^{L-1} w^2(j) \tag{8}$$

$$\hat{P}(f_n) = \frac{1}{K} \sum_{k=1}^K I_k(f_n) \tag{9}$$

where  $A_k(n)$  represents the finite Fourier transforms of the windowed sequence  $x_k(j)w(j)$ ,  $I_k(f_n)$  represents the corresponding modified periodogram, and  $U$  represents the factor of window weight. The spectral estimation  $\hat{P}(f_n)$  was then obtained from the average of the periodograms.

#### 3.2. Temporal Coherence Analysis for Tonal Signals

The persistent narrowband tonal sounds at distinct frequencies that are radiated from ship machinery are typically present over long time durations and hence, are highly temporally coherent. These tonal sounds can be detected and quantified using temporal coherence calculations [40]. As the tonal signals have energies that are confined to relatively narrow frequency bands and centered at certain frequencies over long time durations, the signals in adjacent time periods are highly correlated at those tonal frequencies. Here, the magnitude-

squared coherence  $MSC$  [55,56] between two adjacent time-windowed signals was first calculated as a function of signal frequency:

$$MSC_{x_w, x_{w+1}}(f) = \frac{|P_{x_w, x_{w+1}}(f)|^2}{P_{x_w, x_w}(f)P_{x_{w+1}, x_{w+1}}(f)}, \tag{10}$$

where  $x_w(t)$  and  $x_{w+1}(t)$  represent signals in two adjacent time windows  $w$  and  $w + 1$ . Then, the cross-power spectral density  $P_{x_w, x_{w+1}}$  and the power spectral densities  $P_{x_w, x_w}$  and  $P_{x_{w+1}, x_{w+1}}$  were estimated using Welch’s averaged modified periodogram method, as shown in Equations (5)–(9).

Next, the temporal coherence in one data unit could be obtained as the averaged magnitude-squared coherence  $MSC$ :

$$TC(f) = \frac{1}{N - 1} \sum_{w=1}^{N-1} MSC_{x_w, x_{w+1}}(f), \tag{11}$$

where  $N$  is the total window number in one data unit. The tonal components were obtained from the peaks of temporal coherence plotted as a function of frequency  $TC(f)$ . Additionally, variable window sizes could be chosen to provide variable frequency resolutions within different frequency ranges.

### 3.3. Frequency-Modulated Tonal Signal Analysis

At high frequencies, tonal signals have been found to have large frequency oscillations around their center frequencies [48] because they have been frequency-modulated (FM). To analyze these FM tonal signals, tone tracks of these signals in spectrograms are extracted. Tone tracks describe the time variation of the fundamental frequency of the tonal signal [57,58]. To estimate the modulation frequency, DC offset is first removed from the tone tracks of FM tonal signals. Then, by applying a Fourier transform on the resulting tone track, the dominant modulation frequency is obtained from the peak.

### 3.4. Spectral Coherence Analysis for Cyclostationary Cavitation Noise

A ship’s rotating propellers generate cavitation noise that is amplitude-modulated [9] or cyclostationary and has hidden periodicities or repetitive patterns, for instance, periodic energy flow [59,60]. This kind of signal is spectrally coherent, inherently arising from interfering spectral components spaced apart by the fundamental and harmonic frequencies of the propeller rotation [40]. Spectral coherence analysis provides an approach for determining the cyclic frequencies. It is based on spectral correlation, defined as the Fourier transform of the cyclic auto-correlation function [61]:

$$S_x^\alpha(f) = \int_{-\infty}^{\infty} R_x^\alpha(\tau) e^{-i2\pi f\tau} d\tau \tag{12}$$

$$R_x^\alpha(\tau) = \int_{-\infty}^{\infty} x(t - \frac{\tau}{2}) x^*(t + \frac{\tau}{2}) e^{-i2\pi\alpha t} dt \tag{13}$$

where  $R_x^\alpha(\tau)$  is the cyclic auto-correlation function of signal  $x(t)$  at cyclic frequency  $\alpha$  and  $S_x^\alpha(f)$  is the corresponding spectral correlation.

The fast spectral correlation estimator  $S_x^{Fast}(\alpha, f)$  [60] was utilized to estimate the spectral correlation, which has been proven to have a great statistical performance along with the advantage of rapid computation, where  $\alpha$  represents cyclic frequency and  $f_c$  represents carrier frequency:

$$S_x^{Fast}(\alpha, f) = \frac{\sum_{p=0}^P S_x(\alpha, f; p)}{\sum_{p=0}^P R_w(\alpha - p\Delta f)} R_w(0) \tag{14}$$

$$S_x(\alpha, f_k; p) = \frac{1}{K\|w\|^2 F_s} \sum_{i=0}^{K-1} X_{STFT}(i, f_k) X_{STFT}^*(i, f_{k-p}) e^{-j2\pi \frac{\alpha}{F_s} (iR+N_0)} e^{j2\pi \frac{pN_0}{N_w}} \tag{15}$$

$$= \frac{1}{K\|w\|^2 F_s} DFT_{i \rightarrow \alpha} \{ X_{STFT}(i, f_k) X_{STFT}^*(i, f_{k-p}) \} e^{-j2\pi N_0 (\frac{\alpha}{F_s} - \frac{p}{N_w})} \tag{16}$$

$$\alpha = p\Delta f + \delta \tag{17}$$

$$R_w(\alpha) = \sum_{n=0}^{N_w-1} |w[n]|^2 e^{-j2\pi(n-N_0) \frac{\alpha}{F_s}} \tag{18}$$

$$X_{STFT}(i, f_k) = \sum_{m=0}^{N_w-1} x[iR+m] w[m] e^{-j2\pi m \frac{f_k}{F_s}} \tag{19}$$

where  $S_x(\alpha, f_k; p)$  represents the “scanning spectral correlation”, which estimates spectral correlation from the discrete Fourier transform of the interactions between the STFT coefficients in frequency bins  $f_k$  and  $f_{p-k}$ , not necessarily spaced apart by exact  $\alpha$  but by  $p\Delta f$ , which is the closet frequency bin to  $\alpha$  with some residue  $\delta$ , in order to smoothly envelope the wave packet.  $R_w(\alpha)$  represents the window kernel from window function  $w$  with a central time index at  $N_0$ .  $K$  is the number of windows,  $N_w$  is the window length, and  $P$  is the maximum value of  $p$ . Based on this estimator, the spectral coherence  $\gamma_x(\alpha, f_c)$  could be obtained:

$$S_x(\alpha, f_c) = S_x^{Fast}(\alpha, f_c) \tag{20}$$

$$\gamma_x(\alpha, f_c) = \left| \frac{S_x(\alpha, f_c)}{\sqrt{S_x(f_c) S_x(f_c - \alpha)}} \right| \tag{21}$$

The mean spectral coherence  $\gamma_x(\alpha)$  in the cyclic frequency  $\alpha$  domain was obtained by averaging across the carrier frequency  $f_c$ :

$$\gamma_x(\alpha) = \frac{1}{N_{f_c}} \sum_{f_c} \gamma_x(\alpha, f_c). \tag{22}$$

The periodicities in propeller cavitation noise energy flow could be estimated from the peak components of the mean spectral coherence, corresponding to rotation frequencies including harmonics of ship’s propellers.

#### 4. Results of the Ship Noise Analysis

##### 4.1. Ship Energetics via Power Spectral Density Analysis

The power spectral density calculations revealed the ship’s cylinder firing rate *CFR*. The spectrogram analyses based on the short-time Fourier transform of the recorded data and the corresponding power spectral density are shown in Figure 2a–d, respectively, for the fixed propeller pitch ratio of 65%. Ship noise was dominant in the measured data from 0 Hz to 3 kHz and could be significant up to 30 kHz at and near the closest point of approach. The ship-radiated sound included narrowband machinery tonal signals and broadband propeller cavitation noise. The sequence of click signals around 50 kHz was due to the ship’s echo-sounder (see Figure 2a). At and near the closest point of approach, Lloyd’s mirror effects were present in the measurements (Figure 2b) and the tonal signals were most dominant.

A series of harmonic tonal signals were present in the PSD distributions (see Figure 2d). The fundamental frequency could be estimated from the spacings between adjacent harmonic components, estimated to be around 6.3 Hz, and corresponded to the cylinder

firing rate *CFR*. These *CFR* harmonics could only be detected from the seventh harmonic onwards, which was around 44.1 Hz. The strongest *CFR* component was located at 56.7 Hz, corresponding to the ninth harmonic. This component was slightly larger than the theoretical first harmonic component of the engine firing rate *EFR* that occurs at the eighth harmonic of *CFR*. As a result, *EFR* and hence, the cylinder number as the ratio of *EFR* and *CFR* could not be accurately estimated.

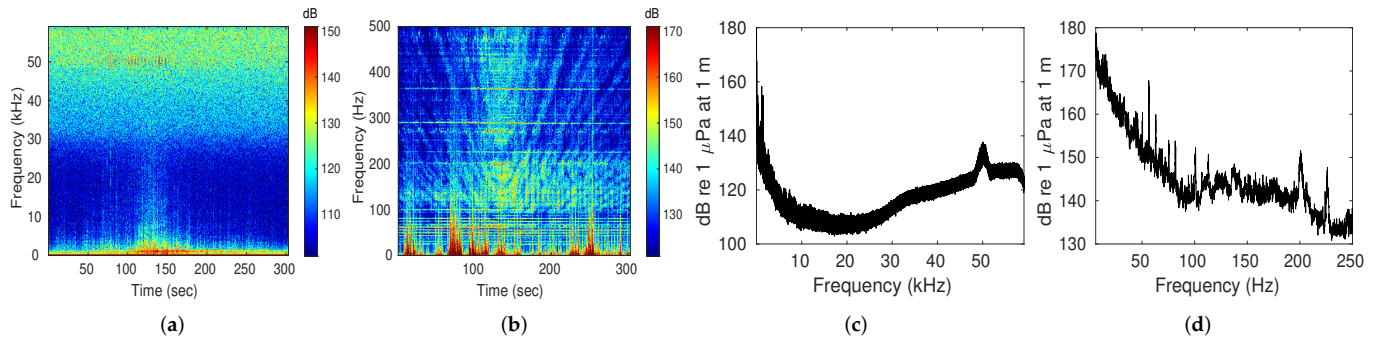


**Figure 2.** The power spectrum of ship-radiated underwater sound at 65% propeller pitch ratio. The spectrograms of acoustic signals (a) up to 60 kHz and (b) below 500 Hz, obtained by short-time Fourier transform. The power spectral density (PSD) distributions of a signal (c) up to 60 kHz and (d) below 250 Hz. Window = 16 s; overlap = 8 s; fft points =  $2^{21}$ ;  $\Delta f = 0.0625$  Hz.

#### 4.2. Ship Tonal Signals via Temporal Coherence Analysis

The ship’s tonal signal components were determined via temporal coherence analysis in Figure 3. Here, three window sizes were used to provide different frequency resolutions in distinct frequency ranges. At higher frequency ranges, a wider frequency resolution was used since the tonal signals there have larger frequency oscillations. The temporal coherence calculations detrended the data so that the *CFR* tonal frequency components could be revealed more readily than in the PSD distribution (compare Figure 3a to Figure 2d).

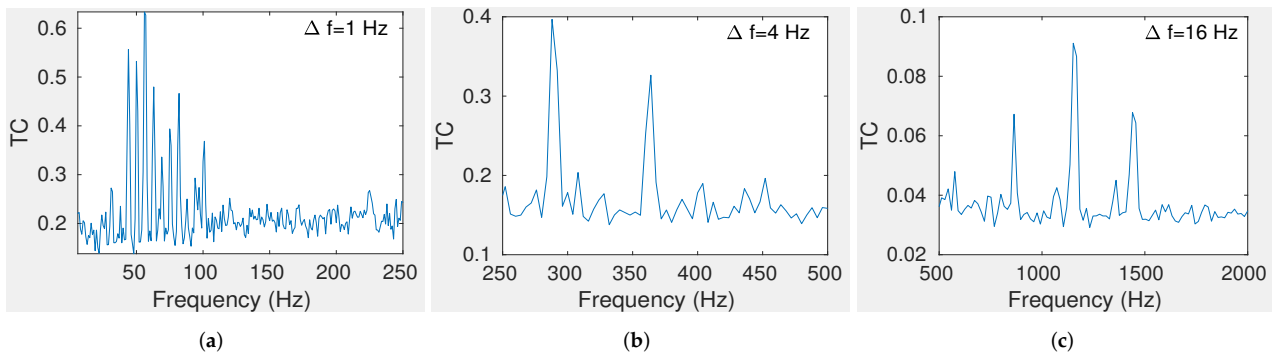


**Figure 3.** The temporal coherence *TC* distribution of ship-radiated underwater sound at 65% propeller pitch ratio and at frequencies (a) below 250 Hz with  $\Delta f = 1$  Hz, (b) between 250 Hz and 500 Hz with  $\Delta f = 4$  Hz, and (c) between 500 Hz and 2000 Hz with  $\Delta f = 16$  Hz. The 7th to 13th harmonics of cylinder firing rate *CFR* are prominent in (a).

#### 4.3. Cyclostationary Cavitation Noise via Spectral Coherence Analysis

The spectral coherence analysis of the ship-radiated sound enabled both the propeller blade pass frequency *BPF* and shaft frequency *SF* to be determined, the ratio of which was the blade number. The two-dimensional spectral coherence distribution as a function of cyclic frequency ( $\alpha$ ) and carrier frequency ( $f_c$ ) from the analysis of the recorded data is shown in Figure 4a. The dominant spectral coherence (SC) values were located between 10 kHz and 40 kHz in the carrier frequency  $f_c$  corresponding to the ship’s propeller cavitation noise and around 50 kHz in carrier frequency  $f_c$  corresponding to echo sounder signals. The mean spectral coherence obtained by averaging the entire carrier frequency  $f_c$  range is



shown in Figure 4b. By selecting different averaging intervals in carrier frequency  $f_c$ , the spectral coherence means for the echo-sounder signals and the ship’s propeller noise could be separated, as shown in Figure 4c,d, respectively. The harmonic group shown in Figure 4c had a fundamental frequency of 2.885 Hz, which corresponded to the ship’s echo-sounder transmission rate. The harmonic group shown in Figure 4d had a fundamental frequency of 3.384 Hz, which corresponded to the propeller shaft frequency  $SF$ . Furthermore, the propeller blade pass frequency  $BPF$  given by the most dominant component shown in Figure 4d was 13.54 Hz and corresponded to the fourth harmonic of the shaft frequency  $SF$ . Hence, the propeller blade number could be estimated to be 4. These estimates were in good or exact agreement with the values provided in Tables 2 and 4 for the known ship’s parameters.

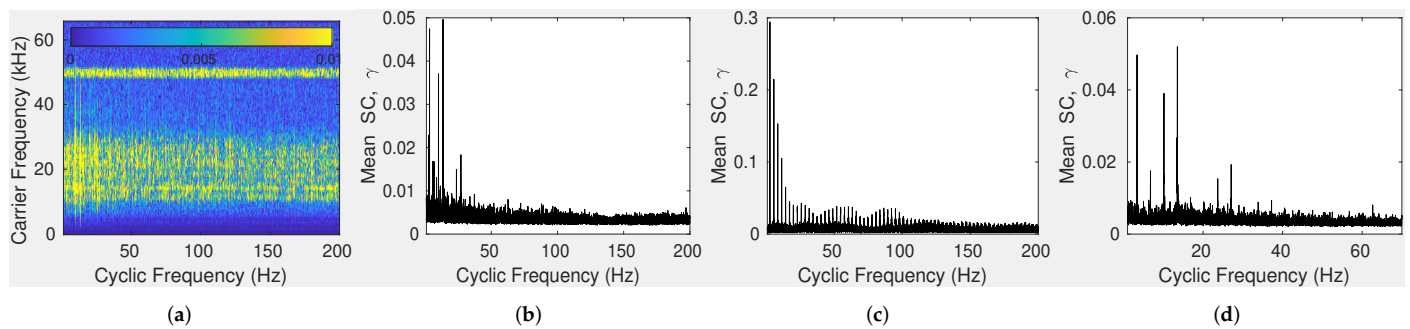


**Figure 4.** The spectral coherence (SC) of ship-radiated underwater sound at 82% pitch. (a) The spectral coherence  $\gamma(\alpha, f_c)$  plotted as function of cyclic frequency  $\alpha$  and carrier frequency  $f_c$ . The mean spectral coherence  $\gamma(\alpha)$  distributions plotted as a function of cyclic frequency  $\alpha$  by averaging (b) the entire carrier frequency  $f_c$  range, (c) between 48 kHz and 52 kHz in the carrier frequency  $f_c$  range, and (d) the entire carrier frequency  $f_c$  range, excluding 48 kHz to 52 kHz. The ship’s cyclostationary cavitation noise shaft frequency  $SF$  first to fourth harmonics are prominent in (d).

## 5. A Comparison of the Ship’s Sound Characteristics at Different Propeller Pitches

### 5.1. Power at Different Propeller Pitches

Here, we compare the ship-radiated underwater sound power spectral density (PSD) levels at seven different propeller pitches. For signals between 100 Hz and 2000 Hz, the PSD level was the strongest at a 20% propeller pitch ratio (Figure 5a). The PSD then decreased with the increase in pitch until 51% pitch, where it was at a minimum, after which the PSD level increased with the increase in pitch. The PSD level below 250 Hz showed more complex variations with pitch (see Figure 5b). For instance, the 20% pitch led to the lowest PSD levels below 75 Hz. The differences were due to the different kinds of cavitation taking place at the propeller. For a detailed analysis of the different noise emissions of each cavitation phenomenon, see [50].

### 5.2. Tonal Signal Variations at Different Propeller Pitches

The power spectral density (PSD) level and temporal coherence values  $TC$  are plotted for significant tonal signals, i.e., the 7th to 13th harmonics of  $CFR$ , as a function of propeller pitch ratios in Figure 6a,b. The ninth harmonic of  $CFR$  had the highest PSD level and  $TC$  value at every propeller pitch. The PSD level of all harmonic tonals of  $CFR$  varied only slightly, between 2 dB to 4 dB with changes in pitch, with the exception of eighth harmonic where its PSD level changed by as much as 10 dB with variations in pitch, but still remained below the PSD level of the ninth harmonic. The temporal coherence values  $TC$  for most of the  $CFR$  tonals were high or at the maximum at 51% propeller pitch. This could be explained by the fact that the cavitation noise spectra was shifted toward higher frequencies above 500 Hz for the 51% propeller pitch, as can be noted from Figure 5b. Consequently, the tonal components below 100 Hz emerged more clearly in the spectrum.

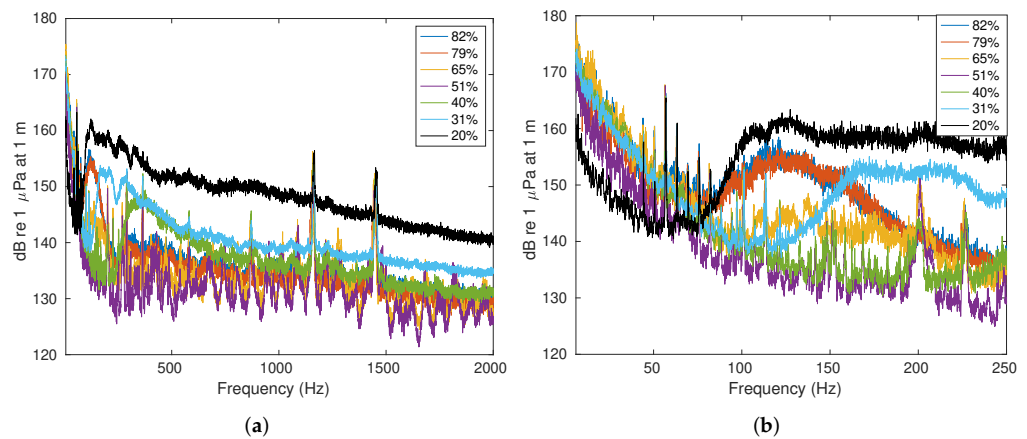


**Figure 5.** The power spectral density (PSD) distributions of ship-radiated underwater sound (a) up to 2000 Hz and (b) below 250 Hz at different propeller pitch ratios.

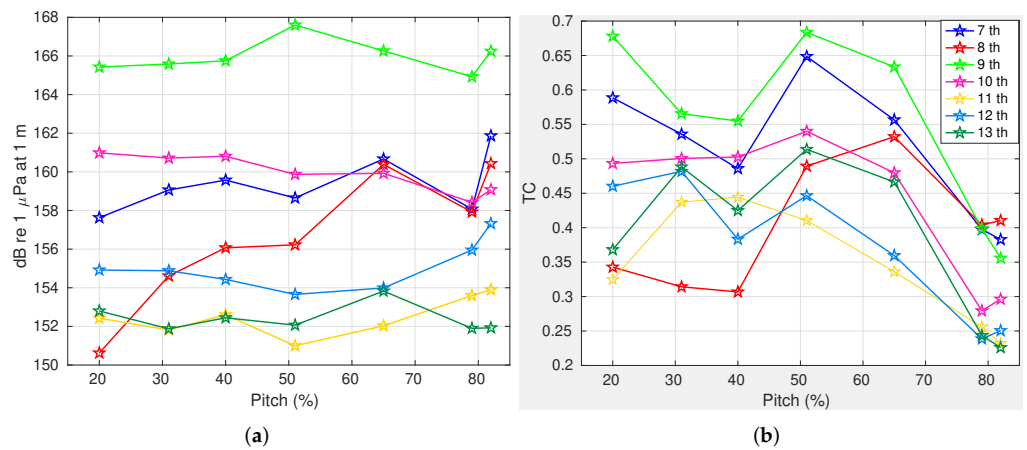


**Figure 6.** The (a) power spectral density (PSD) and (b) temporal coherence  $TC$  of the dominant 7th to 13th tonal harmonics of the cylinder firing rate (CFR) at different propeller pitch ratios.

Frequency-modulated (FM) tonal signal features are also compared at different propeller pitches in this paper. Figure 7 shows a spectrogram containing two narrowband FM tonal signals with frequencies wavering in the ranges of 1435–1460 Hz and 1145–1170 Hz, respectively. The mean and standard deviation of the frequency of these two FM tonal signals are plotted as functions of propeller pitch ratios in Figure 8a,b. The mean frequencies of both FM tonal signals could vary by 10 Hz with changes in propeller pitch and were consistently low between 60% and 80% pitch. The standard deviations of FM tonal frequencies were also the largest at high propeller pitch. The modulation frequencies of these FM tonal signals were the largest near 50% pitch, implying that the signal tone frequencies fluctuated the most at this pitch (see Figure 8c).

### 5.3. Propeller Cavitation Noise at Different Pitches

Next, propeller cavitation noise is compared at different propeller pitches via spectral coherence. The mean spectral coherence  $\gamma(\alpha)$  distribution of propeller cavitation noise plotted as a function of cyclic frequency  $\alpha$  is shown in Figure 9a–g for different propeller pitches. Table 5 summarizes the capacity for the estimation of the ship’s propeller parameters from spectral coherence distributions at different propeller pitches, where  $SF1$ – $SF4$  are the first to fourth harmonics of shaft frequency and the fourth harmonic of shaft frequency  $SF4$  is the propeller blade pass frequency  $BPF$ .

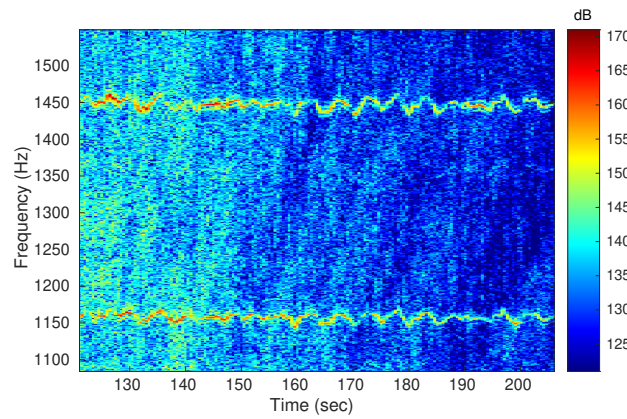


**Figure 7.** The spectrogram of the ship-radiated underwater sound at 82% propeller pitch ratio, showing two frequency-modulated (FM) narrowband tonal signals wavering within the frequency ranges of 1435–1460 Hz and 1145–1170 Hz.

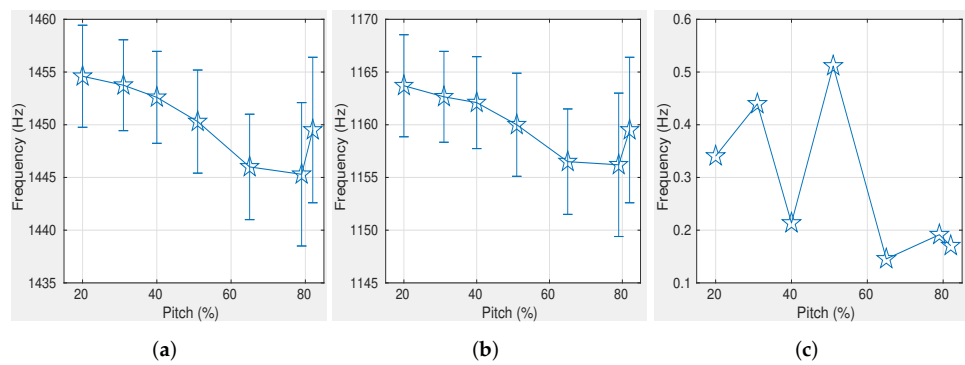


**Figure 8.** The mean and standard deviation of frequency variations in ship-radiated underwater FM tonal signals, (a) within 1435–1460 Hz and (b) within 1145–1170 Hz, at different propeller pitch ratios. (c) The modulation frequency of FM tonal signals at different propeller pitch ratios.

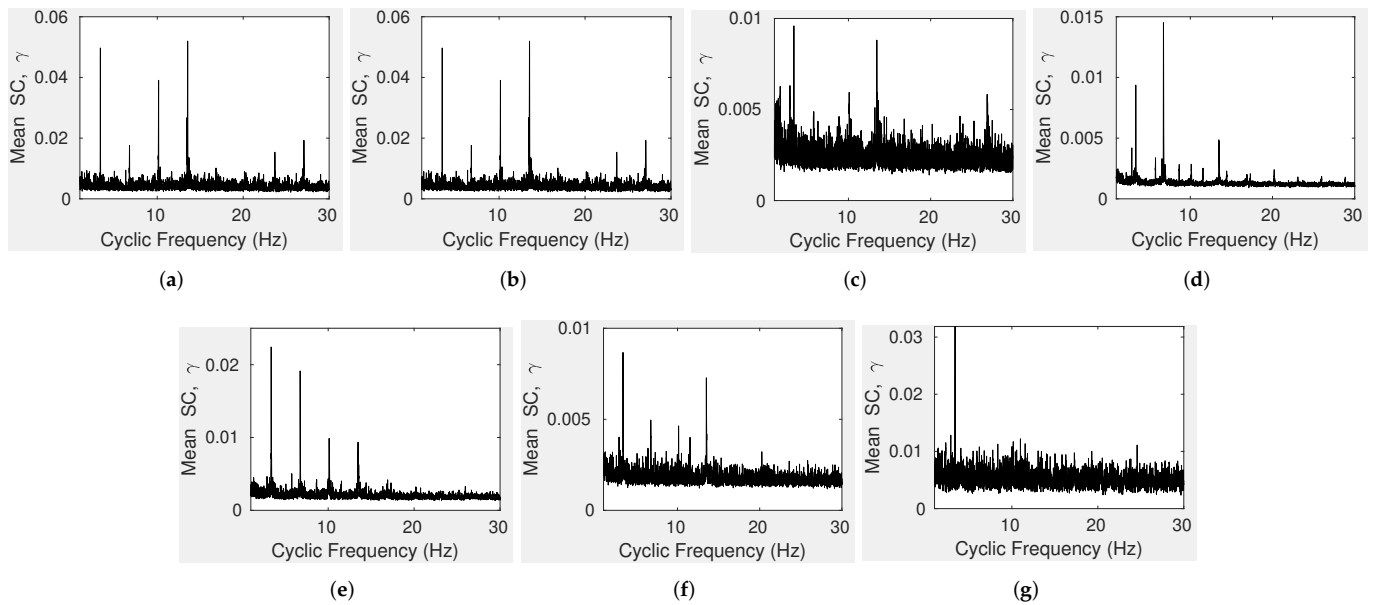


**Figure 9.** The mean spectral coherence (SC)  $\gamma(\alpha)$  distributions plotted as a function of cyclic frequency  $\alpha$  for propeller cavitation noise with pitch ratios at (a) 82%, (b) 79%, (c) 65%, (d) 51%, (e) 40%, (f) 31%, and (g) 20%.

The mean spectral coherence  $\gamma(\alpha)$  distributions were ideal at 82% and 79% pitches, as shown in Figure 9a, since the propeller shaft frequency  $SF$ , blade pass frequency  $BPF$ , and blade number could be readily and correctly estimated. These propeller parameters could also be estimated at 65% and 31% pitches, but the mean spectral coherence values were smaller by a factor of four to six. At 65% pitch, the second harmonic of shaft frequency  $SF2$  could not be identified (Figure 9c). At other pitch ratios, the situation was far from ideal. At 51% pitch, the second harmonic of shaft frequency  $SF2$  was much larger than the fundamental  $SF1$  and the blade pass frequency  $BPF$ , which was  $SF4$ , implying that the correct blade number could not be estimated (Figure 9d). At 40% pitch, the magnitudes of the first four shaft frequency harmonics decreased with the increase in harmonic order (Figure 9e), so both blade pass frequency  $BPF$  and blade number were uncertain. The worst case scenario occurred at 20% pitch (Figure 9g), since only the fundamental shaft frequency  $SF1$  could be identified. This could be due to pressure side cavitation taking place for negative angles of attack. Such an operative condition was very far from the designed one and the broadband cavitation noise was very high, as can also be seen from the black curve in Figure 5b for 20% pitch.

**Table 5.** The efficacy and robustness of the estimation of propeller parameters.

Pitch (%)	82	79	65	51	40	31	20
SF1 (SF)	✓	✓	✓	✓	✓	✓	✓
SF2	✓	✓	×	✓	✓	✓	×
SF3	✓	✓	✓	✓	✓	✓	×
SF4 (BPF)	✓	✓	✓	✓	✓	✓	×
Blade Number	✓	✓	✓	×	×	✓	×

✓ represents predictable and × represents unpredictable.

The dependence of the spectral coherence on the carrier frequency  $f_c$  at shaft frequencies provides further insights into ship propeller cavitation noise [62]. For several representative pitch ratios, the spectral coherences of the first four shaft frequency harmonics  $SF1-SF4$  are plotted as functions of carrier frequency  $f_c$  in Figure 10a–d. At 82% pitch, both the first and fourth harmonics of shaft frequency,  $SF1$  and  $SF4$ , had high spectral coherence values in the carrier frequency  $f_c$  range from 10 kHz to 30 kHz. The second and third harmonics of shaft frequency,  $SF2$  and  $SF3$ , had comparatively low coherence values in the same carrier frequency range but were still significant. This scenario ensured that the propeller parameters could be estimated correctly. At the other pitches shown in Figure 10b–d, the fourth harmonic of shaft frequency  $SF4$  was consistently weak or similar in magnitude to the other harmonics, so propeller blade pass frequency and blade number could be harder to infer.

The spectral coherence  $\gamma(\alpha, f_c)$  as a function of carrier frequency  $f_c$  at seven distinct propeller pitch ratios are plotted separately for the first four shaft frequency harmonics in Figure 11a–d, respectively. The spectral coherence behavior was similar at 82% and 79% pitches, with significantly higher values for the first, third, and fourth harmonics of shaft frequency, which led to the estimation of propeller parameters with high confidence. The behavior at 65% and 31% pitches were similar, but with significantly lower spectral coherence values. The spectral coherence values were low for all pitches at the fourth harmonic of shaft frequency, except for the idealized cases of 82% and 79% pitches.

#### 5.4. Robustness of the Estimation of Ship Parameters

Here, we summarize the robustness of the estimation of the ship’s parameters from the underwater radiated sound at different propeller pitches.

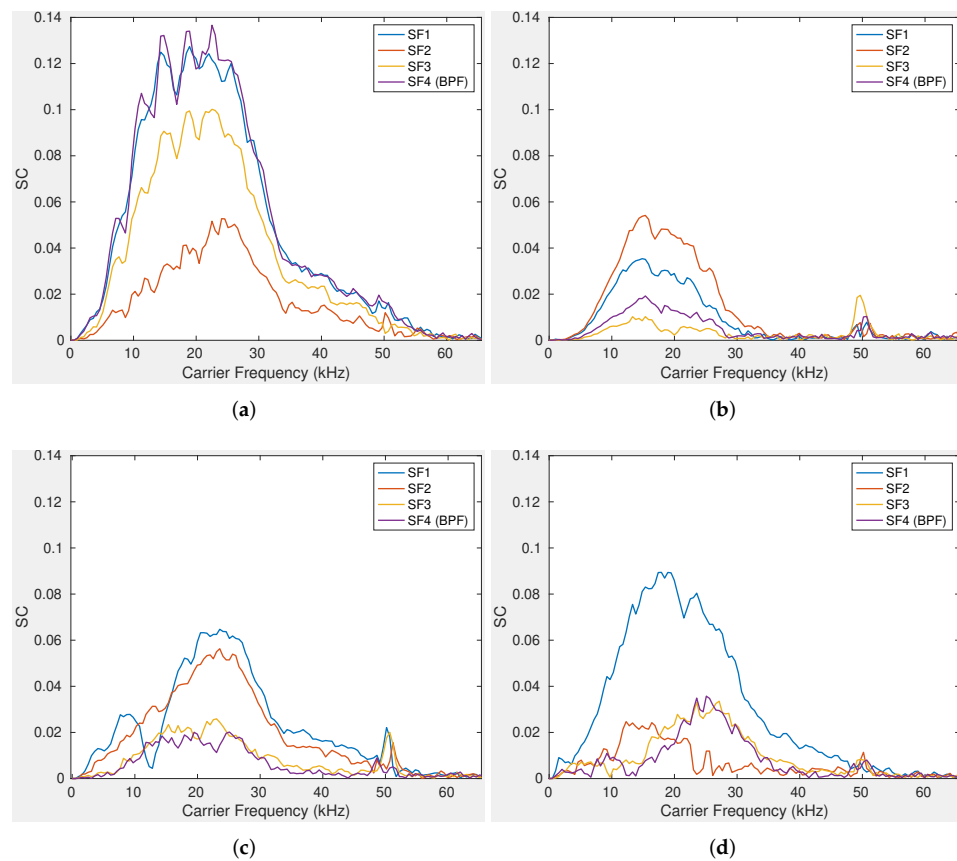


**Figure 10.** The spectral coherences (SC)  $\gamma(\alpha, f_c)$  of propeller cavitation noise across the entire carrier frequency  $f_c$  range at the first four harmonics of shaft frequency,  $\alpha = SF1, SF2, SF3, SF4$ , with propeller pitch ratios at (a) 82%, (b) 51%, (c) 40%, and (d) 20%.

#### 5.4.1. Engine-Related Parameters

Among the various engine-related parameters, only the cylinder firing rate  $CFR$  could be well estimated at different pitches from the differences in adjacent harmonic frequencies since the fundamental  $CFR$  component was not detected. Under normal conditions, the engine firing rate  $EFR$  can be estimated to be the strongest harmonic component of  $CFR$ , whose order number is the number of cylinders in the engine [9,63,64]. However, in this analysis,  $EFR$  could not be correctly estimated for this ship since the corresponding eighth harmonic was not the strongest tonal harmonic of  $CFR$ . However, the ninth harmonic of  $CFR$  was found to be the dominant tonal, both in terms of the highest power and the highest temporal coherence at every propeller pitch, as shown in Figure 6. As a result, the correct cylinder number could not be estimated, but was probably near to nine (the cylinder number provided for the ship under study is eight in Table 3).

#### 5.4.2. Propeller-Related Parameters

Propeller-related parameters, such as shaft frequency  $SF$ , blade pass frequency  $BPF$ , and blade number, can be estimated from the spectral coherence distributions of ship-radiated cavitation noise [4,9,45,46,62,65]. The magnitude of the spectral coherence at one specific frequency represents how dominant the corresponding time period is, at which propeller blades generate cavitation noise. In other words, it indicates how many propeller blades generate cavitation noise at approximately the same time for each rotation cycle and whether these blades generate cavitation noise with uniform time intervals between rotation cycles.

$SF$  can be obtained as the fundamental frequency of the spectral coherence distribution, if at least one blade generates cavitation noise with a uniform time interval. Under perfect conditions, especially when all propeller blades generate cavitation noise at approximately

the same time during each propeller rotation cycle, *BPF* can be estimated to be the second strongest harmonic component after *SF*. Then, the blade number can be obtained as the harmonic order of *BPF* with respect to *SF*. However, under other scenarios, especially when different propeller blades generate cavitation noise at different time instants during each rotation cycle or only few blades generate cavitation noise, then *BPF* and the blade number cannot be properly estimated, since the spectral coherence at *BPF* is no longer outstanding among the harmonics of *SF* [4,62].

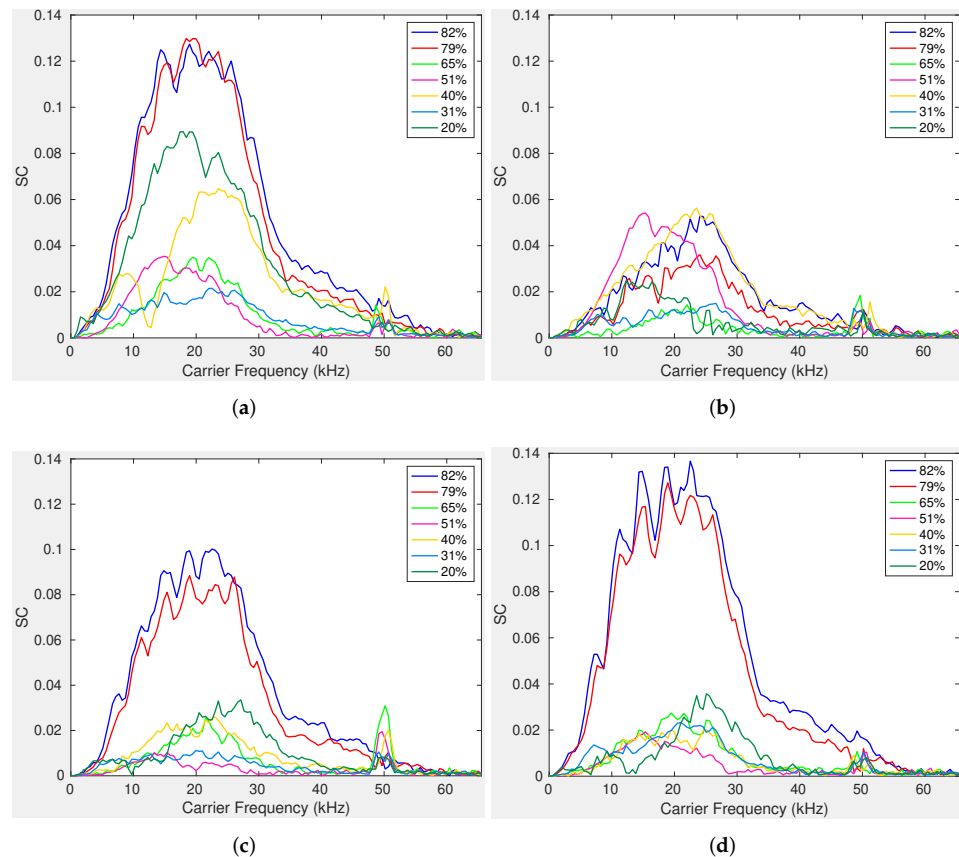


**Figure 11.** The spectral coherences (SC)  $\gamma(\alpha, f_c)$  of the (a) first,  $\alpha = SF1$ , (b) second,  $\alpha = SF2$ , (c) third,  $\alpha = SF3$ , and (d) fourth,  $\alpha = SF4$ , harmonics of shaft frequency across the entire carrier frequency  $f_c$  range at different propeller pitch ratios, ranging from 20% to 82%.

As shown in Figure 9 and Table 5, the shaft frequency *SF* could be obtained at all propeller pitches analyzed here, which means there was always at least one blade generating cavitation noise with the change of propeller pitch. However, the blade pass frequency *BPF* and blade number might not be correctly estimated. The most challenging scenario was at 20% pitch, where only the shaft frequency *SF* could be obtained. This indicates that, at this pitch, only one blade generated cavitation noise, but with a uniform time interval.

#### 5.4.3. Gear-Related Parameters

Gear-related parameters can also be obtained, which is the reduction gear rate *RGR*. According to Equations (1)–(4), after the shaft frequency *SF* and cylinder firing rate *CFR* are estimated, the reduction gear rate *RGR* can be obtained from the ratio of those two [9,62]. However, there are multiple possibilities due to different engine stroke numbers. For a 2-stroke engine, the reduction gear rate is calculated as  $RGR = CFR/SF$ . For a 4-stroke engine, the reduction gear rate is obtained as  $RGR = CFR \cdot 2/SF = 6.3 \cdot 2/3.384 = 3.723$ , which matches the gear parameter for the ship under study in Table 3.

### 5.5. Changes in Both Propeller Pitch and RPM

Here, we analyze and discuss one special measurement where the ship changed speed, and both propeller pitch and RPM. The ship’s speed changed continuously while propeller RPM underwent a jump over the measurement time window, as shown in Figure 12a,b. The ship continuously increased speed from 5.5 knots to 12.5 knots. The shaft frequency  $SF$  hovered around 3.37 Hz for the initial 3/4 of the measurement time window and then increased to 3.8 Hz for the remaining 1/4. The jump in shaft frequency was a result of the jump increase in propeller RPM. Detailed propeller pitch information is not available for this measurement.

The power spectral density (PSD), temporal coherence  $TC$ , and mean spectral coherence  $\gamma(\alpha)$  for this special measurement are shown in Figure 13a–c, respectively. The dominant tonal at 56.8 Hz had the largest PSD and  $TC$ , similar to previous results, corresponding to the ninth harmonic of  $CFR$  associated with a shaft frequency of 3.37 Hz and a lower propeller RPM of 760. Due to the longer measurement time at low RPM (3/4 of the measurement duration), the tonal signals were dominant at frequencies associated with low RPM. The mean spectral coherence distribution, however, displayed harmonic groups corresponding to shaft frequency  $SF$  of 3.8 Hz instead, which was associated with a higher RPM of approximately 860. This result implies that the cavitation noise at high RPM was significantly stronger and more dominant than that at low RPM, despite the smaller measurement time at high RPM (only 1/4 of the measurement duration).

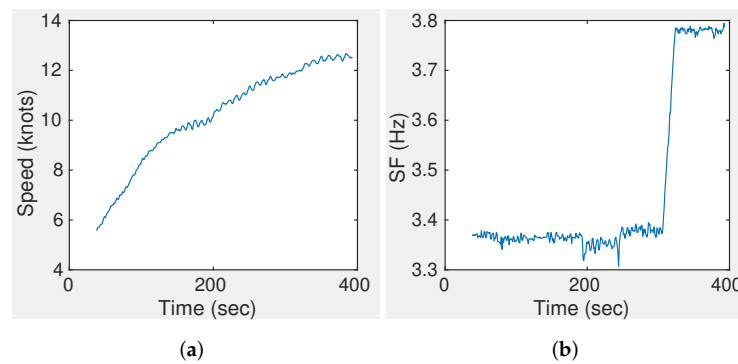


**Figure 12.** (a) Ship speed and (b) fundamental propeller shaft frequency  $SF_1$  change with time when the ship changed both propeller revolutions per minute (RPM) and propeller pitch ratios.

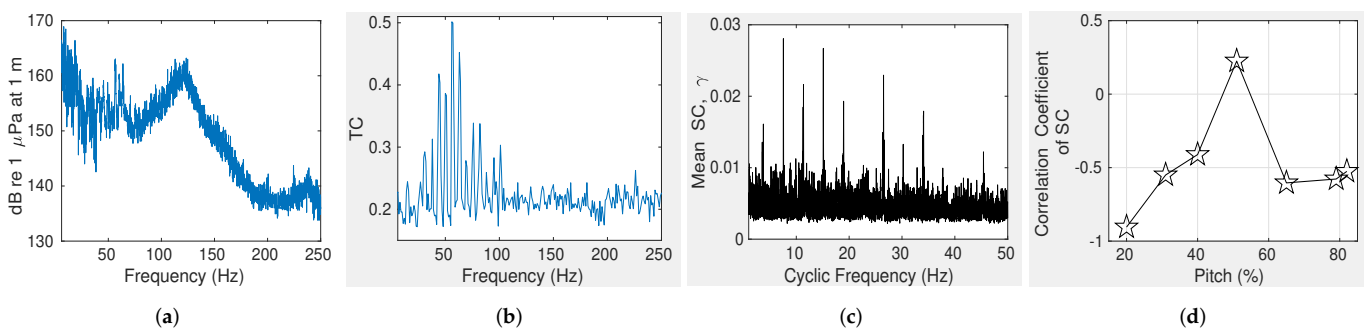


**Figure 13.** The (a) power spectral density (PSD), (b) temporal coherence  $TC$ , and (c) mean spectral coherence (SC)  $\gamma(\alpha)$  distributions of ship-radiated underwater sound when the ship changed both propeller RPM and pitch ratios. (d) The correlation coefficients between the mean spectral coherence values in (c) and those at different pitch ratios in Figure 9, with respect to the first four harmonics of shaft frequency  $SF$ .

The mean spectral coherence variation with the increase in harmonic order, shown in Figure 13c, was similar to that of Figure 9d, corresponding to 51% pitch, following an “increase–decrease–increase” trend among the first four harmonics of shaft frequency  $SF$ . The correlation coefficient between the mean spectral coherence values for the first four

harmonics of shaft frequency for the special measurement here, shown in Figure 13c, and at different pitches, shown in Figure 9a–g, were calculated and plotted in Figure 13d. The highest correlation for the special case here was with the 51% pitch. This indicates that the most dominant propeller pitch for the special measurement here could be around 51%. Besides the first four harmonics of shaft frequency, the mean spectral coherence distribution for the special measurement, shown in Figure 13c, also clearly revealed higher order shaft frequency harmonics, ranging from the fifth to the ninth, and twelfth.

## 6. Discussion

The underwater sound radiated by a ship with a controllable pitch propeller (CPP) was analyzed and quantified as a function of propeller pitch ratio, including acoustic feature extraction and ship parameter estimation. The ship's acoustic signature was characterized in terms of (i) signal energetics via power spectral density, (ii) machinery tonal sound via temporal coherence, (iii) propeller cavitation noise via spectral coherence, and (iv) frequency-modulated (FM) tonal signal mean and standard deviation in frequency variation. Each of these quantities were calculated from ship-radiated underwater sound measurement at different propeller pitch ratios, ranging from 20% to 80%, and then compared.

The 51% pitch was found to be a crucial point for this ship, because (a) the power spectral density of the radiated sound reached the lowest levels over a broad range of frequencies, (b) the power spectral density and temporal coherence of the ship's significant tonal sounds attained their highest values, and (c) the modulation frequency of the FM tonal signals were the largest. However, the spectral coherences of shaft frequency harmonics for the ship's cavitation noise were among the lowest at 51% pitch.

The efficacy and robustness of the estimation of the ship's parameters under different propeller pitch ratios were investigated. Our analysis indicates that the cylinder firing rate *CFR* could be well estimated at all propeller pitches from the frequency differences in adjacent *CFR* tonal harmonics. The engine firing rate *EFR* and cylinder number could not be accurately estimated since the strongest *CFR* harmonic was found to be one order higher than that provided for the ship under study. The propeller shaft frequency (*SF*) could be obtained from the spectral coherence analysis of the cavitation noise at every propeller pitch. The blade pass frequency (*BPF*) and blade number could be estimated for several pitches, but not all. The reduction gear rate (*RGR*) could be calculated from the *CFR* and *SF* frequencies with an appropriate engine stroke number assumption. The shaft frequency harmonics were most coherent at 79% and 82% pitches, providing the ideal distributions for estimating the blade pass frequency, blade number, and reduction gear rate of the ship.

An analysis of one special measurement where ship changed speed, propeller pitch and RPM over the course of the measurement indicates that the cavitation noise at high RPM was significantly stronger than at low RPM.

These findings elucidate the effects of pitch variation on underwater sound radiated by a specific ship with a controllable pitch propeller, which brings some valuable insights into ship propeller design and operation. However, in order to obtain a much deeper and more accurate understanding of underwater sound from ships with controllable pitch propellers, more analyses should be conducted on a sufficient number of ships. More factors should also be taken into account, including ship type, ship tonnage, ship speed, engine type, propeller shape, propeller size, propeller material, etc.

**Author Contributions:** Conceptualization, data curation, formal analysis, methodology, and investigation, C.Z., T.G. and P.R.; software and visualization, C.Z.; writing—original draft, C.Z.; writing—review and editing, C.Z., T.G. and P.R.; funding acquisition, P.R.; supervision, N.C.M. All authors have read and agreed to the published version of the manuscript.

**Funding:** This research was supported by the US Office of Naval Research (Ocean Acoustics Program) and the US National Science Foundation.

**Institutional Review Board Statement:** Not applicable.



**Informed Consent Statement:** Not applicable.

**Data Availability Statement:** Data sharing not applicable.

**Conflicts of Interest:** The authors declare no conflict of interest.

## References

1. Bergmann, P.G.; Major, J.; Wildt, R. *Physics of Sound in the Sea*; Gordon and Breach: London, UK, 1968.
2. Arveson, P.T.; Vendittis, D.J. Radiated noise characteristics of a modern cargo ship. *J. Acoust. Soc. Am.* **2000**, *107*, 118–129. [[CrossRef](#)] [[PubMed](#)]
3. Bruno, M.; Chung, K.; Salloum, H.; Sedunov, A.; Sedunov, N.; Sutin, A.; Graber, H.; Mallas, P. Concurrent use of satellite imaging and passive acoustics for maritime domain awareness. In Proceedings of the Waterside Security Conference (WSS), 2010 International, Carrara, Italy, 3–5 November 2010.
4. Chung, K.W.; Sutin, A.; Sedunov, A.; Bruno, M. DEMON acoustic ship signature measurements in an urban harbor. *Adv. Acoust. Vib.* **2011**, *2011*. [[CrossRef](#)]
5. Fillinger, L.; Sutin, A.; Sedunov, A. Acoustic ship signature measurements by cross-correlation method. *J. Acoust. Soc. Am.* **2010**, *129*, 774–778. [[CrossRef](#)] [[PubMed](#)]
6. Leal, N.; Leal, E.; Sanchez, G. Marine vessel recognition by acoustic signature. *ARPN J. Eng. Appl. Sci.* **2015**, *10*, 9633–9639.
7. Ogden, G.L.; Zurk, L.M.; Jones, M.E.; Peterson, M.E. Extraction of small boat harmonic signatures from passive sonar. *J. Acoust. Soc. Am.* **2011**, *129*, 3768–3776. [[CrossRef](#)]
8. Wales, S.C.; Heitmeyer, R.M. An ensemble source spectra model for merchant ship-radiated noise. *J. Acoust. Soc. Am.* **2002**, *111*, 1211–1231. [[CrossRef](#)]
9. Urick, R.J. *Principles of Underwater Sound*, 3rd ed.; Peninsula Publishing: Los Atlos, CA, USA, 1983.
10. Makris, N.C.; Ratilal, P.; Symonds, D.T.; Jagannathan, S.; Lee, S.; Nero, R.W. Fish population and behavior revealed by instantaneous continental shelf-scale imaging. *Science* **2006**, *311*, 660–663. [[CrossRef](#)]
11. Makris, N.C.; Ratilal, P.; Jagannathan, S.; Gong, Z.; Andrews, M.; Bertsatos, I.; Godø, O.R.; Nero, R.W.; Jech, J.M. Critical population density triggers rapid formation of vast oceanic fish shoals. *Science* **2009**, *323*, 1734–1737. [[CrossRef](#)]
12. Wang, D.; Garcia, H.; Huang, W.; Tran, D.D.; Jain, A.D.; Yi, D.H.; Gong, Z.; Jech, J.M.; Godø, O.R.; Makris, N.C.; et al. Vast assembly of vocal marine mammals from diverse species on fish spawning ground. *Nature* **2016**, *531*, 366–370. [[CrossRef](#)]
13. Duane, D.; Cho, B.; Jain, A.D.; Godø, O.R.; Makris, N.C. The Effect of Attenuation from Fish Shoals on Long-Range, Wide-Area Acoustic Sensing in the Ocean. *Remote Sens.* **2019**, *11*, 2464. [[CrossRef](#)]
14. Garcia, H.A.; Zhu, C.; Schinault, M.E.; Kaplan, A.I.; Handegard, N.O.; Godø, O.R.; Ahonen, H.; Makris, N.C.; Wang, D.; Huang, W.; et al. Temporal–spatial, spectral, and source level distributions of fin whale vocalizations in the Norwegian Sea observed with a coherent hydrophone array. *ICES J. Mar. Sci.* **2019**, *76*, 268–283. [[CrossRef](#)]
15. Mohebbi-Kalkhoran, H.; Zhu, C.; Schinault, M.; Ratilal, P. Classifying humpback whale calls to song and non-song vocalizations using bag of words descriptor on acoustic data. In Proceedings of the 2019 18th IEEE International Conference On Machine Learning And Applications (ICMLA), IEEE, Boca Raton, FL, USA, 16–19 December 2019; pp. 865–870.
16. Seri, S.G.; Zhu, C.; Schinault, M.; Garcia, H.; Handegard, N.O.; Ratilal, P. Long Range Passive Ocean Acoustic Waveguide Remote Sensing (POAWRS) of Seismo-Acoustic Airgun Signals Received on a Coherent Hydrophone Array. In Proceedings of the OCEANS 2019 MTS/IEEE SEATTLE, Seattle, WA, USA, 27–31 October 2019; pp. 1–8.
17. MacLennan, D.N.; Simmonds, E.J. *Fisheries Acoustics*; Springer Science & Business Media: Berlin/Heidelberg, Germany, 2013; Volume 5.
18. Vieira, M.; Amorim, M.; Sundelöf, A.; Prista, N.; Fonseca, P.J. Underwater noise recognition of marine vessels passages: Two case studies using hidden Markov models. *ICES J. Mar. Sci.* **2019**, *77*, 2157–2170. [[CrossRef](#)]
19. Duane, D.; Zhu, C.; Piavsky, F.; Godø, O.R.; Makris, N.C. The Effect of Attenuation from Fish on Passive Detection of Sound Sources in Ocean Waveguide Environments. *Remote Sens.* **2021**, *13*, 4369. [[CrossRef](#)]
20. Stojanovic, M. Underwater acoustic communications. In Proceedings of the Electro/95 International, Professional Program Proceedings, Boston, MA, USA, 21–23 June 1995; pp. 435–440.
21. Stojanovic, M.; Preisig, J. Underwater acoustic communication channels: Propagation models and statistical characterization. *IEEE Commun. Mag.* **2009**, *47*, 84–89. [[CrossRef](#)]
22. Dambra, R.; Firenze, E. Underwater radiated noise of a small vessel. In Proceedings of the 22nd International Congress on Sound and Vibration, Florence, Italy, 12–16 July 2015; pp. 12–16.
23. Hildebrand, J.A. Anthropogenic and natural sources of ambient noise in the ocean. *Mar. Ecol. Prog. Ser.* **2009**, *395*, 5–20. [[CrossRef](#)]
24. Merchant, N.D.; Witt, M.J.; Blondel, P.; Godley, B.J.; Smith, G.H. Assessing sound exposure from shipping in coastal waters using a single hydrophone and Automatic Identification System (AIS) data. *Mar. Pollut. Bull.* **2012**, *64*, 1320–1329. [[CrossRef](#)]
25. Vasconcelos, R.O.; Amorim, M.C.P.; Ladich, F. Effects of ship noise on the detectability of communication signals in the Lusitanian toadfish. *J. Exp. Biol.* **2007**, *210*, 2104–2112. [[CrossRef](#)]
26. Slabbekoorn, H.; Dooling, R.J.; Popper, A.N.; Fay, R.R. *Effects of Anthropogenic Noise on Animals*; Springer: Berlin/Heidelberg, Germany, 2018.

27. Codarin, A.; Wysocki, L.E.; Ladich, F.; Picciulin, M. Effects of ambient and boat noise on hearing and communication in three fish species living in a marine protected area (Miramare, Italy). *Mar. Pollut. Bull.* **2009**, *58*, 1880–1887. [[CrossRef](#)]
28. Ona, E.; Godø, O.R.; Handegard, N.O.; Hjellvik, V.; Patel, R.; Pedersen, G. Silent research vessels are not quiet. *J. Acoust. Soc. Am.* **2007**, *121*, EL145–EL150. [[CrossRef](#)]
29. Mitson, R. Underwater noise radiated by research vessels. *ICES Mar. Sci. Symp.* **1993**, *196*, 147–152.
30. Mitson, R.B.; Knudsen, H.P. Causes and effects of underwater noise on fish abundance estimation. *Aquat. Living Resour.* **2003**, *16*, 255–263. [[CrossRef](#)]
31. Hawkins, A.D.; Pembroke, A.E.; Popper, A.N. Information gaps in understanding the effects of noise on fishes and invertebrates. *Rev. Fish Biol. Fish.* **2015**, *25*, 39–64. [[CrossRef](#)]
32. Veirs, S.; Veirs, V.; Wood, J.D. Ship noise extends to frequencies used for echolocation by endangered killer whales. *PeerJ* **2016**, *4*, e1657. [[CrossRef](#)]
33. Erbe, C.; Dunlop, R.; Dolman, S. Effects of noise on marine mammals. In *Effects of Anthropogenic Noise on Animals*; Springer: Berlin/Heidelberg, Germany, 2018; pp. 277–309.
34. Fréchou, D.; Dugué, C.; Briançon-Marjollet, L.; Fournier, P.; Darquier, M.; Descotte, L.; Merle, L. Marine Propulsor Noise Investigations in the Hydroacoustic Water Tunnel “GTH”. In Proceedings of the Twenty-Third Symposium on Naval Hydrodynamics, Val de Reuil, France, 17–22 September 2000; Office of Naval Research Bassin d’Essais des Carenes National Research Council: Washington, DC, USA, 2001.
35. Bush, V.; Conant, J.B.; Tate, J.T. *Principles and Applications of Underwater Sound*; Technical Report; Office of Scientific Research and Development: Washington, DC, USA, 1946; Volume 7.
36. Norwood, C. An introduction to ship radiated noise. *Acoust. Aust.* **2002**, *30*, 21–25.
37. Ojak, W. Vibrations and waterborne noise on fishery vessels. *J. Ship Res.* **1988**, *32*, 112–133. [[CrossRef](#)]
38. Gray, L.M.; Greeley, D.S. Source level model for propeller blade rate radiation for the world’s merchant fleet. *J. Acoust. Soc. Am.* **1980**, *67*, 516–522. [[CrossRef](#)]
39. Grelowska, G.; Kozaczka, E.; Kozaczka, S.; Szymczak, W. Underwater noise generated by a small ship in the shallow sea. *Arch. Acoust.* **2013**, *38*, 351–356. [[CrossRef](#)]
40. Zhu, C.; Seri, S.G.; Mohebbi-Kalkhoran, H.; Ratilal, P. Long-range automatic detection, acoustic signature characterization and bearing-time estimation of multiple ships with coherent hydrophone array. *Remote Sens.* **2020**, *12*, 3731. [[CrossRef](#)]
41. Zhu, C. Remote Monitoring of Multiple Ships over Instantaneous Continental-Shelf Scale Region with Large-Aperture Coherent Hydrophone Array. Ph.D. Thesis, Northeastern University, Boston, MA, USA, 2020.
42. Malinowski, S.J.; Gloza, I. Underwater noise characteristics of small ships. *Acta Acust. United Acust.* **2002**, *88*, 718–721.
43. Gloza, I. Identification Methods of Underwater Noise Sources Generated by Small Ships. *Acta Phys. Pol. A.* **2011**, *119*. [[CrossRef](#)]
44. McKenna, M.F.; Ross, D.; Wiggins, S.M.; Hildebrand, J.A. Underwater radiated noise from modern commercial ships. *J. Acoust. Soc. Am.* **2012**, *131*, 92–103. [[CrossRef](#)] [[PubMed](#)]
45. Antoni, J.; Hanson, D. Detection of surface ships from interception of cyclostationary signature with the cyclic modulation coherence. *IEEE J. Ocean. Eng.* **2012**, *37*, 478–493. [[CrossRef](#)]
46. Hanson, D.; Antoni, J.; Brown, G.; Emslie, R. Cyclostationarity for ship detection using passive sonar: Progress towards a detection and identification framework. In Proceedings of the ACOUSTICS 2009, Adelaide, SA, Australia, 23–25 November 2009; pp. 1–8.
47. Zhu, C.; Garcia, H.; Kaplan, A.; Schinault, M.; Handegard, N.O.; Godø, O.R.; Huang, W.; Ratilal, P. Detection, localization and classification of multiple mechanized ocean vessels over continental-shelf scale regions with passive ocean acoustic waveguide remote sensing. *Remote Sens.* **2018**, *10*, 1699. [[CrossRef](#)]
48. Huang, W.; Wang, D.; Garcia, H.; Godø, O.R.; Ratilal, P. Continental shelf-scale passive acoustic detection and characterization of diesel-electric ships using a coherent hydrophone array. *Remote Sens.* **2017**, *9*, 772. [[CrossRef](#)]
49. Gaggero, T.; Rizzuto, E.; Traverso, F.; Trucco, A. Comparing ship underwater noise measured at sea with predictions by empirical models. In Proceedings of the 21st International Congress on Sound and Vibration, Beijing, China, 13–17 July 2014; pp. 1510–1516.
50. Traverso, F.; Gaggero, T.; Tani, G.; Rizzuto, E.; Trucco, A.; Viviani, M. Parametric analysis of ship noise spectra. *IEEE J. Ocean. Eng.* **2016**, *42*, 424–438. [[CrossRef](#)]
51. Traverso, F.; Gaggero, T.; Rizzuto, E.; Trucco, A. Spectral analysis of the underwater acoustic noise radiated by ships with controllable pitch propellers. In Proceedings of the OCEANS 2015-Genova, Genova, Italy, 18–21 May 2015; pp. 1–6.
52. AQUO. Achieve QUIeter Oceans by Shipping Noise Footprint Reduction. Available online: [www.aquo.eu](http://www.aquo.eu) (accessed on 8 January 2022).
53. ANSI/ASA. S12.64-2009/Part 1, Quantities and Procedures for Description and Measurement of Underwater Sound from Ship—Part 1: General Requirements. 2009. Available online: <https://webstore.ansi.org/standards/asa/ansiasas12642009part1> (accessed on 8 January 2022).
54. Welch, P. The use of fast Fourier transform for the estimation of power spectra: A method based on time averaging over short, modified periodograms. *IEEE Trans. Audio Electroacoust.* **1967**, *15*, 70–73. [[CrossRef](#)]
55. Goodman, J. *Statistical Optics*; Wiley: New York, NY, USA, 1988.
56. Kay, S.M. *Modern Spectral Estimation*; Prentice Hall: Hoboken, NJ, USA, 1988.
57. Shapiro, A.D.; Wang, C. A versatile pitch tracking algorithm: From human speech to killer whale vocalizations. *J. Acoust. Soc. Am.* **2009**, *126*, 451–459. [[CrossRef](#)]

58. Baumgartner, M.F.; Mussoline, S.E. A generalized baleen whale call detection and classification system. *J. Acoust. Soc. Am.* **2011**, *129*, 2889–2902. [[CrossRef](#)]
59. Antoni, J. Cyclostationarity by examples. *Mech. Syst. Signal Process.* **2009**, *23*, 987–1036. [[CrossRef](#)]
60. Antoni, J.; Xin, G.; Hamzaoui, N. Fast computation of the spectral correlation. *Mech. Syst. Signal Process.* **2017**, *92*, 248–277. [[CrossRef](#)]
61. Gardner, W. Measurement of spectral correlation. *IEEE Trans. Acoust. Speech Signal Process.* **1986**, *34*, 1111–1123. [[CrossRef](#)]
62. Pollara, A.; Sutin, A.; Salloum, H. Improvement of the Detection of Envelope Modulation on Noise (DEMON) and its application to small boats. In Proceedings of the OCEANS 2016 MTS/IEEE Monterey, Monterey, CA, USA, 19–23 September 2016; pp. 1–10.
63. Boashash, B.; O'shea, P. A methodology for detection and classification of some underwater acoustic signals using time-frequency analysis techniques. *IEEE Trans. Acoust. Speech Signal Process.* **1990**, *38*, 1829–1841. [[CrossRef](#)]
64. Pollara, A.; Sutin, A.; Salloum, H. Modulation of high frequency noise by engine tones of small boats. *J. Acoust. Soc. Am.* **2017**, *142*, EL30–EL34. [[CrossRef](#)]
65. Hanson, D.; Antoni, J.; Brown, G.; Emslie, R. Cyclostationarity for passive underwater detection of propeller craft: A development of DEMON processing. In Proceedings of the Acoustics 2008, Geelong, VIC, Australia, 24–26 November 2008; pp. 24–26.